

Dopant Segregation in Polycrystalline Monolayer Graphene

Liuyan Zhao,[†] Rui He,^{†,‡} Amir Zabet-Khosousi,[§] Keun Soo Kim,^{†,||} Theanne Schiros,[⊥] Michael Roth,^{‡,¶} Philip Kim,^{†,▽} George W. Flynn,[§] Aron Pinczuk,^{†,▽} and Abhay N. Pasupathy^{*,†}

[†]Department of Physics, Columbia University, New York, New York 10027, United States

[‡]Department of Physics, University of Northern Iowa, Cedar Falls, Iowa 50614, United States

[§]Department of Chemistry, Columbia University, New York, New York 10027, United States

^{||}Department of Physics and Graphene Research Institute, Sejong University, Seoul 143-747, Korea

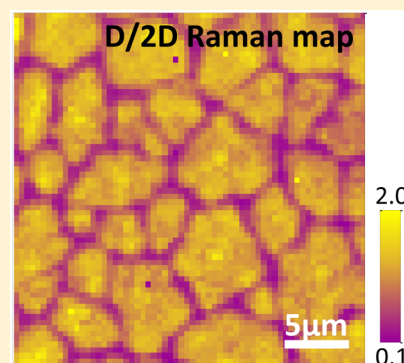
[⊥]Energy Frontier Research Center, Columbia University, New York, New York 10027, United States

[¶]Department of Physics and Geology, Northern Kentucky University, Highland Heights, Kentucky 41099, United States

[▽]Department of Applied Physics and Applied Mathematics, Columbia University, New York, New York 10027, United States

Supporting Information

ABSTRACT: Heterogeneity in dopant concentration has long been important to the electronic properties in chemically doped materials. In this work, we experimentally demonstrate that during the chemical vapor deposition process, in contrast to three-dimensional polycrystals, the substitutional nitrogen atoms avoid crystal grain boundaries and edges over micron length scales while distributing uniformly in the interior of each grain. This phenomenon is universally observed independent of the details of the growth procedure such as temperature, pressure, substrate, and growth precursor.



KEYWORDS: Chemical vapor deposition, nitrogen-doped graphene, dopant segregation, micro-Raman spectroscopy, scanning tunneling microscopy

Doping, alloying, and functionalization are common strategies by which the electronic properties of materials can be tuned. In three-dimensional (3D) polycrystalline materials such as metals,¹ ceramics,^{2,3} and semiconductors,^{4–9} atomic impurities, and dopants are known to migrate toward surfaces and grain boundaries during high-temperature annealing processes, resulting in an inhomogeneous modification of electronic and structural properties of the material. Such chemical segregation is of great practical importance in applications as diverse as structural steels,¹ electronics,^{5,8,10,11} and electrochemical cells.¹² The chemical segregation can be understood as a two-step process. First, elevated temperatures used during annealing leads to enhanced diffusion, allowing foreign atoms to reach the grain boundary.¹³ Second, electronic interactions between hydrogenic states of the dopant atom and the boundary states leads to binding of the dopant at the boundary.^{14,15} These processes typically lead to the aggregation of dopants at the grain boundary with a length scale of a few lattice constants.^{1–9,11,12}

Recently, it has become possible to create large-area, true 2D (monolayer) materials by chemical vapor deposition (CVD) techniques. When grown by CVD, all of these materials grow as a patchwork quilt of microcrystalline grains separated by edges

and grain boundaries.^{16,17} The fast expanding set of materials that can be grown this way include graphene,^{18–21} hexagonal boron nitride,^{22,23} and transition metal dichalcogenides.^{24,25} These unique 2D materials are being explored for a host of applications including electronics, sensors, and catalysis. Chemical doping or alloying is a natural method that has been explored to tune their electronic, mechanical, and chemical properties.²⁶ The interplay between dopants and impurities with the edges or grain boundaries present in these films is unexplored. Diffusion in 2D materials is a surface phenomenon that includes several mechanisms that are not present in bulk 3D diffusion.^{27,28} Further, grain boundaries are 1D objects in a 2D material, while they are 2D surfaces in a 3D material. We thus expect dimensionality to play a key role in the diffusion of dopant atoms to a grain boundary as well as in the electronic interaction between dopants and grain boundaries.

To study the functionalization process in such 2D materials, we choose N-doped monolayer graphene produced by CVD on

Received: December 18, 2014

Revised: January 14, 2015

Published: January 27, 2015

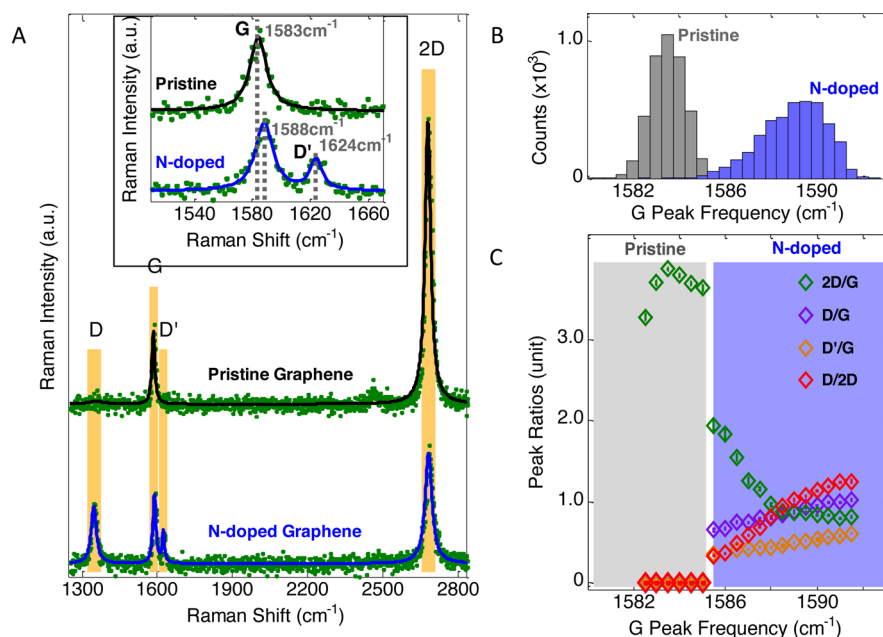


Figure 1. Raman spectra and statistics of pristine and N-doped graphene films. (A) Raman spectrum of pristine (black) and of N-doped (blue) graphene films with D, G, D', and 2D peak positions highlighted in yellow background. The inset shows a zoom-in plot in the range of G and D' peaks. (B) Statistics of G peak frequencies on pristine (gray) and N-doped (blue) graphene samples over $25 \times 25 \text{ } (\mu\text{m})^2$ areas. (C) Statistical relations between peak intensity ratios including D/G, D'/G, 2D/G, and D/2D with respect to G peak frequency.

a copper substrate,^{19,20} which is a well-characterized member of this family. Microscopic measurements of this functionalized material have already revealed its atomic-scale doping forms and local electronic properties.^{29–32} On the micrometer scale, it is well-known that CVD graphene films are polycrystalline.^{16,17} Therefore, these films are an ideal medium to study the spatial homogeneity of atomic dopants within grains and across grain boundaries. Here we use the high sensitivity of micro-Raman spectroscopy to atomic N dopants and its induced charge carriers in the graphene lattice to map the dopant distribution over large areas of the films with submicron spatial resolution. We complement these measurements with X-ray measurements that give us elemental specificity and bonding information, and atomic-resolution scanning tunneling microscopy (STM) measurements near grain boundaries and edges that provide us with a direct visual probe of dopant concentration at the nanometer scale. The N-doped graphene films in our studies were grown using low-pressure CVD technique on copper substrates^{18,19} with a variety of growth conditions and precursor gases, which are denoted as NG_Xm (recipe (a) with Xm standing for a growth time of X-minute) and NG_Pyridine (recipe (b)), respectively. Details of sample preparation are described in Supporting Information S1. Some of the measurements are conducted on samples with no further preparation (“as-grown”), while other measurements detailed below are performed on films transferred to insulating SiO₂/Si substrates (details of transfer procedure in Supporting Information S2).

In order to confirm the presence and structure of the nitrogen dopants in our N-doped graphene films, we have used multiple analytical tools to characterize the samples. First, we performed X-ray photoelectron spectroscopy (XPS) measurements on both as-grown as well as transferred films to show the presence of N dopants³³ and estimated the N concentration in the N-doped graphene films (Supporting Information S3). In our full coverage samples (NG_10m), the doping level

estimated is 0.4%. Next, to identify the doping form of N dopants across the entire N-doped graphene film, we performed soft X-ray near edge X-ray absorption fine structure (NEXAFS) spectroscopy measurements with its scanning mode (scanning NEXAFS) over the entire sample. In line with previous measurements,³³ we find sharp N 1s-to- π^* and -to- σ^* resonances at ~ 400.8 and 408 eV with strong electric polarization dependence. This provides clear evidence of graphitic N doping form in which an N dopant forms sp^2 bonds with each of its three nearest C neighbors. Using the scanning mode of operation (lateral resolution of $50 \text{ } \mu\text{m}$), we have confirmed that $>90\%$ of all the dopants are in the substitutional form over the entire film (Supporting Information S4). Finally, atomic resolution STM is performed at a large number of spots on N-doped graphene films. STM topography (Supporting Information S5) and spectroscopy, clearly show the substitutional nature of the nitrogen dopant,³⁰ and consistent with the X-ray measurements, we find that $>90\%$ of all defect structures arise from the substitutional nitrogen dopant. The concentration of N dopants extracted from STM measurements ($\sim 0.25\text{--}0.35\%$) is consistent with the other techniques. Thus, all of the analytical techniques indicate consistently that the N dopants in our films are primarily in the graphitic form and in the subpercent range.

While X-ray measurements give us large-scale information on the nature of the dopant, they do not have sufficient spatial resolution to study dopant homogeneity. On the other hand, STM imaging has atomic resolution but cannot be used to survey large areas comparable to the grain size in our films. We thus chose micro-Raman spectroscopy with a diffraction-limited resolution as a technique capable of sufficient spatial resolution along with the ability to survey large areas of the film. Figure 1A shows typical Raman spectra (532 nm laser excitation) taken from a pristine graphene and a NG_10m film on SiO₂/Si substrates. The Raman spectrum from pristine CVD graphene shows sharp and intense G and 2D bands with a 2D/G ratio of

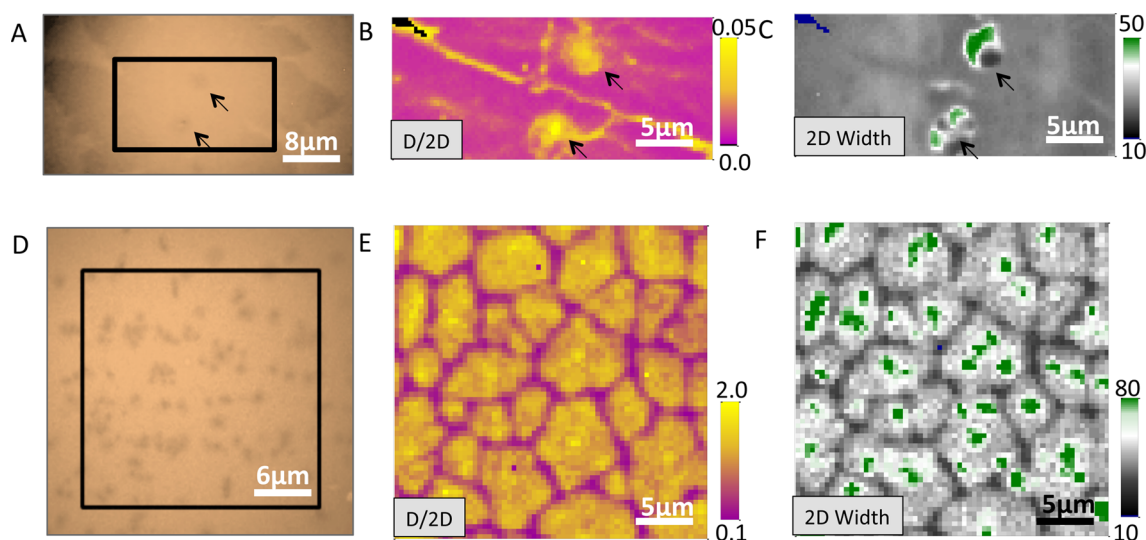


Figure 2. Optical images and Raman maps of pristine and N-doped graphene films. (A–C) Pristine graphene. (A) Optical image of a CVD grown pristine graphene with two seeds highlighted by arrows. (B) Map of the intensity ratio of D/2D Raman bands in the area highlighted by the rectangular box in (a). (C) 2D width map taken at the same area as in (B). (D–F) N-doped graphene with 10 min growth (NG_10m). (D) Optical image of a fully covered NG_10m sample. (E,F) D/2D intensity ratio and 2D width maps in the area highlighted by the box in (D).

~ 4 and a negligible D band, similar to mechanically exfoliated samples.^{34–36} In contrast to pristine graphene, the NG_10m film shows strong D and D' bands in the Raman spectrum, and the intensity of the 2D band is significantly suppressed. The G band frequency displays a blue shift as shown in the inset of Figure 1A.

A comparison between the Raman spectra from our N-doped graphene films and those in the literature on sp^2 -hybridized carbon materials with defects reveals important similarities and differences. Our observation of the D and D' bands is broadly consistent with the presence of defects in graphene lattice,^{35–38} although their intensities have been observed to vary depending on the nature of the defect.^{39–42} Blue shifts of the G band frequency have been observed either due to the presence of charge carriers^{43,44} or compressive strain^{45,46} in graphene. In the N-doped graphene samples, STM topography, together with density function theory (DFT) calculations⁴⁷ and transmission electron microscopy (TEM) measurements,²⁹ indicate that graphitic N dopants stay in the graphene plane with minimal changes in the bond lengths. In particular, DFT calculations show that graphitic nitrogen in graphene perturbs the bond lengths by $<1\%$ and its structural effect is limited to the nearest few lattice sites (details in Supporting Information S6).³⁰ This results in almost no local strain in graphene lattice when compared to other defect forms, and thus we can make the reasonable approximation that the G band frequency shift is a measure of charge carrier density in our N-doped graphene samples. Doping also has an impact on the 2D band. The suppression of 2D band intensity can result from the presence of defects in graphene^{35–38} as well as from free charge carriers.^{43,44} Substitutional doping in carbon nanotubes has been reported to generate a double-peak structure in the 2D band due to the electron and phonon renormalization near the charged impurities.⁴⁸ However, we do not observe a clear splitting in the 2D band in Raman spectra from our samples, which is in line with previous measurements on nitrogen-doped graphene.^{19,20,31,49,50} This interesting difference might stem from geometric differences around N dopants in the two systems and requires further investigation.

Having established the basic features in the Raman spectra of our N-doped samples, we use micro-Raman mapping (64×64 pixels) to probe the dopant homogeneity over $25 \times 25 \mu\text{m}^2$ areas of each sample. The samples show a high degree of spatial inhomogeneity. As a first quantification of the inhomogeneity, Figure 1B shows the statistical distribution of G band frequencies taken over a pristine and an NG_10m sample. The statistical mean of the G band position for sample NG_10m is 1589 cm^{-1} while pristine graphene has an average G band position of 1584 cm^{-1} . Previous STM measurements³⁰ have shown that the NG_10m sample is on average electron doped with a carrier concentration of $\sim 7.5 \times 10^{12} \text{ cm}^{-2}$ and, consistent with angle-resolved photoemission spectroscopy (ARPES) measurements,⁵¹ the ratio of charge carrier density to N dopant concentration is approximately constant ($\sim 0.42 \text{ e/N}$) over a wide range of N concentration. Assuming that the average blue shift of the G band ($\sim 5 \text{ cm}^{-1}$) can be attributed solely to the carrier doping, we can estimate from previous measurements on electrostatically doped graphene^{43,44} that the carrier concentration is $\sim 7.0 \times 10^{12} \text{ cm}^{-2}$ in our film, which is in excellent agreement with the STM results.

Using the aggregated Raman spectra obtained from our mapping measurements, we can gain further insight into the effect of dopants on the characteristic features seen in the Raman spectra. We do this by using the G peak frequency as the independent variable and plot the intensity ratios of the characteristic bands in Raman spectra as a function of G band frequency in Figure 1C for both pristine graphene (left panel) and for NG_10m (right panel). The key observations are (a) both the D/G and D'/G intensities are linearly proportional to the G peak frequency shift; (b) the intensity of 2D peak decreases monotonically with increasing G peak frequency; and (c) the D/2D ratio combines the opposing trend of D/G and 2D/G ratios on the G peak frequency and thus shows the steepest dependence as a function of G peak frequency. The broad qualitative trends of the D, D', and 2D bands as a function of defect density are observed in a number of defective carbon systems reported before^{52,53} but the quantitative numbers for peak intensity ratios are often different from

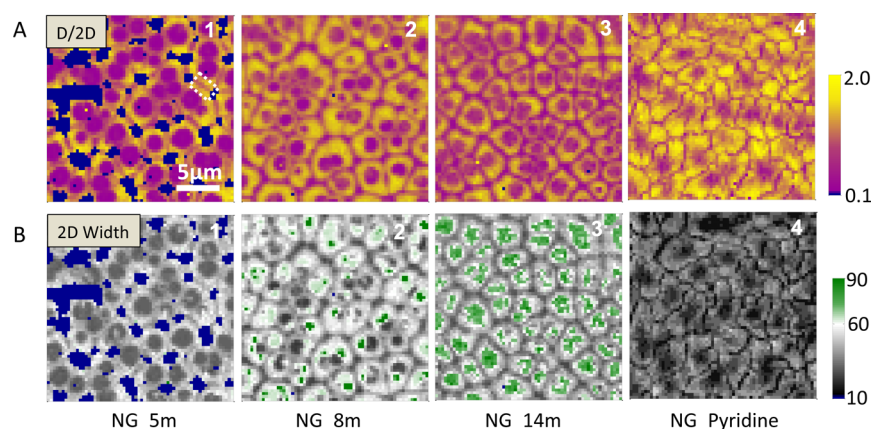


Figure 3. Effect of growth time and precursors on the dopant homogeneity. (A) Maps of the intensity ratios of D/2D Raman bands from NG_5m, NG_8m, NG_14m and NG_pyridine samples. (B) Maps of 2D width taken at the same areas on the same samples as in (A).

other defect forms due to the small size and distortion that graphitic N dopants create. As an example, the D/D' ratio of ~ 2 for the graphitic N dopants is smaller than that observed from other structural defects such as vacancies. This ratio has been used in the past to characterize the nature of defects in graphene.⁴¹ In the limit of large perturbations to the graphene lattice, the D/D' ratio observed is large; this includes D/D' ratios of 13 for out-of plane atoms bonded to C, 10.5 for vacancy-like defects, and 3.5 for grain boundary-like defects.⁴¹ On the other hand, charged impurities such as atoms or molecules that are merely adsorbed on the graphene surface without significant structural disorder are predicted to produce negligible D and D'.⁵⁴ The D/D' ratio of ~ 2 from our N-doped graphene lies in between the two limits, consistent with the idea that the chief role of graphitic N dopants is to add charge to graphene, while creating only small structural disorder in the lattice. A second example is the ratio of intensities of the D peak to the G peak, $I_{D/G}$, which is a function of the dopant concentration ρ_D . Previous measurements on ion-damaged graphene resulted in an empirical model^{52,53} for $I_{D/G}(\rho_D)$ that depends on two fitting parameters, the defect size r_s and range of influence of the defect r_A . Using this model to fit the observed ratios of $I_{D/G}$ from our spectra along with the dopant concentration measured by X-ray and STM measurements requires that the dopant size $r_s \sim 3$ Å and radius of influence $r_A \sim 7$ Å, values that are significantly smaller than that assumed in the literature for other types of defects. These values are however completely consistent with our STM measurements and DFT calculations for the size and influence of the graphitic N dopant.

While there are interesting differences in the Raman spectra between our N-doped samples and other types of defective graphene as noted above, it is very clear from the experiments that the Raman spectrum is very capable of distinguishing between pristine graphene with no defects (intense G and 2D bands with a well-defined frequency and no D and D' bands) and defective graphene (presence of D and D' bands, weakened 2D band and blue-shifted G band). In what follows, we use the Raman maps on our samples to study the interaction between N dopants and the two other sources of structural disorder in CVD graphene, grain boundaries and nucleation seeds. First, we characterize the effect of these structural features on the Raman spectrum of a pristine graphene sample. The nucleation seeds can be directly identified by optical contrast in a microscope, as shown in Figure 2A. The two darker regions

highlighted by arrows are the nucleation seeds of two domains where multilayer graphene is typically found.⁵⁵ We expect a grain boundary to exist in the graphene monolayer between these two seeds. Indeed, Raman spectral maps show evidence for both features as indicated in Figure 2B, which is the D/2D ratio map imaged at the same area highlighted by the black rectangle in Figure 2A. This map shows a line of higher D/2D ratio than the surrounding area, consistent with the presence of a grain boundary.⁵⁶ The existence of multilayers at the nucleation seeds is also confirmed by an image of the 2D bandwidth shown in Figure 2C.^{35,36}

Having understood the effect of grain boundaries and similar structural features on the Raman spectra of pristine graphene, we are now in a position to study the interaction between these structural features and N dopants in chemically doped graphene. Shown in Figure 2E is a D/2D ratio map over a monolayer of NG_10m film (optical image shown in Figure 2D). The map shows a clear patchwork structure as might be expected from a polycrystalline sample. Surprisingly, however, the figure shows that the D/2D intensity is much smaller near the grain boundaries relative to the interior of the grains (which are relatively uniform), in complete contrast to our measurements on pristine graphene. For the NG_10m sample, the average D/2D ratio at the grain boundary is ~ 0.1 , while it is 1.7 in the interior of the grains. This compares to a D/2D ratio of ~ 0.04 at the grain boundary and ~ 0 in the interior for pristine graphene. The surprising conclusion that one reaches from these numbers is that the N dopant concentration at the grain boundaries is much lower than that in the interior, while the interior of the grains is fairly uniformly doped. This conclusion is also supported by the behavior of other features of the Raman spectrum (G peak frequency shift, D/G, D'/G, and 2D/G intensity ratios) as well as by direct STM imaging near the grain boundary (see below).

Natural questions that arise from our observation of dopant inhomogeneity are whether the observed effect of dopant segregation is limited to the grain boundaries, and what the possible role of the growth conditions is on the observed inhomogeneity. To gain further insight into these questions, we grew a series of samples using the same growth process with varying growth times of 5, 8, 10, and 14 min. Using optical microscopy we confirm that the fabricated samples are in a range from a partial monolayer (NG_5m) through a fully formed monolayer (NG_8m, and NG_10m) to a partially formed bilayer (NG_14m). While the basic features are similar

for both as-grown and transferred samples, the transferred samples show better Raman spectra since the background signal is significantly smaller. Shown in Figure 3A(1–3) (D/2D ratio images) and Figure 3B(1–3) (2D width images) are representative data obtained on transferred samples. A clear picture of the evolution of the dopant distribution is obtained from the D/2D ratio images. At short time (NG_5m), the area in the immediate vicinity of the nucleation seed is relatively undoped, while the regions outside the central core are doped. The dopant distribution at the very edge of the individual grains is generally not resolved in the Raman images (with the exception of places where the low N concentration is observed at grain boundaries when two grains merge, such as in the white rectangle area shown in Figure 3A(1)). When the N-doped graphene first forms a complete monolayer (NG_8m), both the nucleation seed and the grain boundary contain less N dopants than the other regions of the film. As time progresses, the doping in the interior of the film becomes more uniform (NG_10m) but the grain boundary remains undoped. For even longer time (NG_14m), large bilayer patches begin to form around the nucleation seeds, but the grain boundaries always stay undoped. On the basis of the fact that the second layer usually grows from the same seed as the first layers⁵⁵ and there is a second layer island within each patch, we can infer that each patch is one structural domain and therefore the regions of low dopant concentration at the boundaries of patches are indeed the structural grain boundaries of graphene. To confirm that these results are not specific to the use of NH_3 as a dopant gas, we have used pyridine as a single precursor to grow N-doped monolayer graphene. Raman spectral maps of this sample (NG_Pyridine) are shown in Figure 3A(4) and Figure 3B(4). These maps clearly exhibit the same basic phenomenology as the ammonia doping process that lower N density is observed at the grain boundaries. The estimated average widths of the N depleted boundaries for samples grown with different times are similar (about 0.6–0.8 μm wide). Meanwhile, the N-doped graphene films grown with pyridine have a narrower width of N depleted region (around 0.5 μm). Estimations of these widths are given in Supporting Information S4. Despite the difference in the absolute values of the widths, all of our samples consistently exhibit lower N concentration at the graphene grain boundaries.

While Raman spectra give us detailed information on defect and doping concentration in graphene films, they do not directly measure the nature of the defects giving rise to the D and D' bands, and the technique is optically limited in spatial resolution to $\sim 0.5 \mu\text{m}$. To complement Raman spectroscopic measurements, we use atomically resolved STM measurements that in the past have been employed to successfully image N dopants in graphene.^{30–32} The room-temperature STM measurements are performed on as-grown N-doped graphene films on Cu foil after annealing at 300 °C for 30 min to improve surface cleanliness.

Shown in Figure 4A is a STM topographic image (displayed in derivative mode) of a $500 \times 500 \text{ nm}^2$ area on a NG_10m sample (raw image is shown in Supporting Information S8). The overall background variations arise from the polycrystalline nature of the copper foil substrate. The graphene monolayer forms a continuous film across this rough terrain. When grains of graphene with different rotational angles or translational shifts merge together, a defect line is usually formed at the grain boundary.^{16,17,57} One such rotational grain boundary is observed in Figure 4a, as highlighted by the black dashed

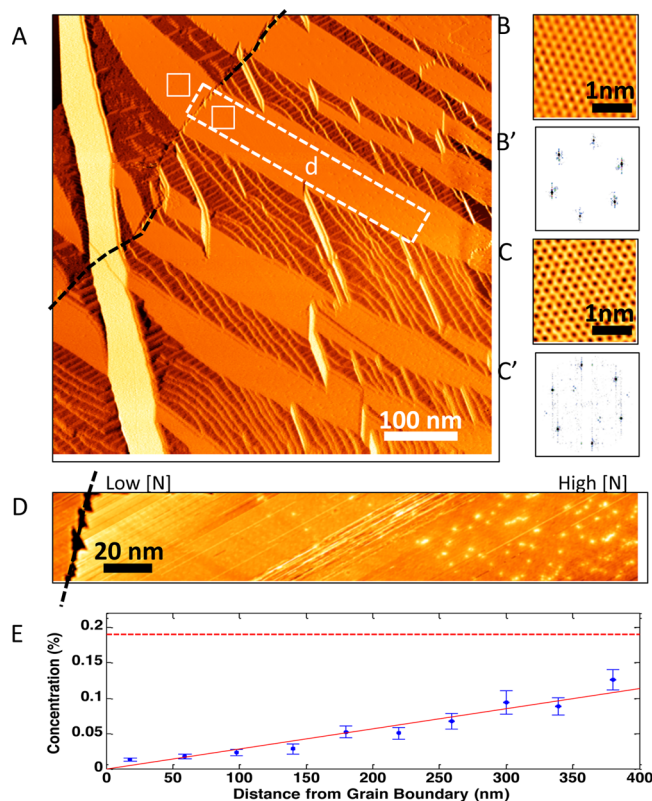


Figure 4. Direct visualization of dopant segregation in large-area graphene by STM. (A) Differential STM image ($500 \text{ nm} \times 500 \text{ nm}$, 1.5 V, 0.1 nA) of an as-grown NG_10m sample. The black dashed line shows the location of a grain-boundary. (B,C) Magnified STM images ($2.6 \text{ nm} \times 2.6 \text{ nm}$, 0.5 V, 10 nA) of the corresponding areas highlighted in (a). Scalebar = 1 nm. (B',C') Fast Fourier transformations of STM images shown in (B,C), respectively. (D) Magnified STM image ($45 \text{ nm} \times 310 \text{ nm}$, 1.5 V, 0.1 nA) of the corresponding highlighted area in (a). (E) N-concentration as a function of distance from the grain boundary. The red solid line is a linear fit to the data. The red dashed line shows the bulk limit of N-concentration in this sample.

line. The crystal orientations of the graphene grains on the two sides of the dashed line are rotated $\sim 18^\circ$ relative to each other as shown in Figure 4B,C. Having located the grain boundary, we can use STM to directly image the dopant concentration as a function of distance from the boundary. Figure 4D shows such an example. In this STM image, N dopants appear as bright features due to an enhancement of the density of states at C sites around N dopants, as reported previously.^{30,32} Close-up STM images obtained with atomic resolution clearly show that the bright spots in Figure 4d are graphitic substitutional N dopants (see Supporting Information S5 and Figure S3 for high resolution image). Figure 4D also clearly shows a depletion of N dopants near the grain boundary, consistent with the Raman results discussed above. We calculated the distance of each dopant atom from the grain boundary and plot the density of the dopants as a function of distance from the grain boundary in Figure 4E. A linear gradient of N dopant concentration is observed, starting from zero at the grain boundary. Given the bulk value of N concentration of $\sim 0.2\%$ for this sample as measured by STM, we estimate the width of the N depleted region near the grain boundary to be $\sim 0.7 \mu\text{m}$. This depletion region width is consistent with Raman measurements on the same sample (NG_10m) described above.

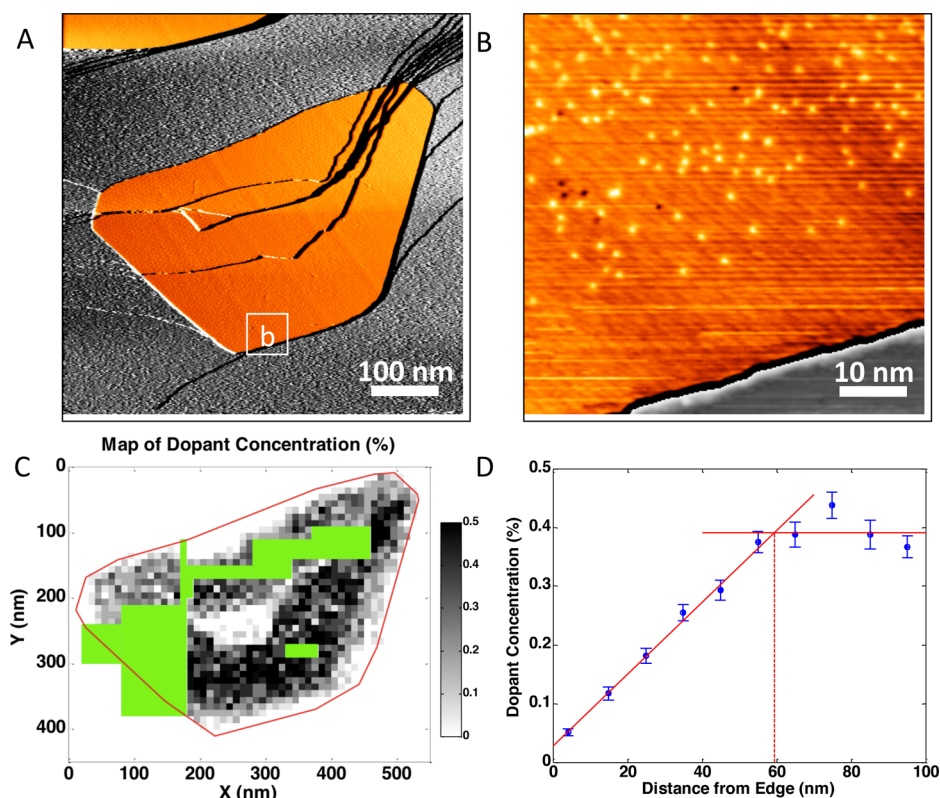


Figure 5. Dopant segregation in nanoscale graphene islands. (A) Differential STM image ($600 \text{ nm} \times 600 \text{ nm}$, 0.5 V , 0.5 nA) of a graphene island. False colors: orange = graphene, gray = copper. (B) Magnified STM image ($60 \text{ nm} \times 60 \text{ nm}$, 0.5 V , 0.5 nA) of the highlighted area in (A). (C) Map of N-distribution across the graphene island. The colorscale represents N-concentration. Red lines represent the edges of the graphene island. Shaded boxes are areas where data are missing. (D) N-concentration as a function of distance from the graphene edge. Red solid lines are linear fits to the data.

To study the effect of the growth conditions, such as temperature and pressure, on the observed dopant inhomogeneity, we fabricated N-doped graphene under completely different growth conditions. We used pyridine vapor as a single precursor under UHV conditions (pyridine pressure of 10^{-4} Torr and base pressure of 10^{-10} Torr) on a single crystal Cu(111) surface between 800 and 950°C , following the procedure for pristine graphene growth.⁵⁸ We can tune the graphene coverage from isolated islands to complete monolayers depending on growth time and study the dopant concentration near edges and boundaries. As an example, we show in Figure 5A a STM topography of a $300 \times 400 \text{ nm}^2$ N-doped graphene island on the stepped surface of Cu(111). The graphene is identified by its apparent height on the Cu substrate in STM image. We carefully studied the distribution of dopants in this island by taking high-resolution STM images across the island. Figure 5B shows one such STM image obtained across one edge of the graphene island in Figure 5A. The bright features seen are the N dopants, and a few dark spots are also seen due to the defects in the underlying Cu substrate. This image directly demonstrates that the N dopants avoid the edge of the island. By taking a sequence of such images, we quantified the N dopant density over the entire island and plot the result in Figure 5C. We can clearly see that the N dopants avoid the edges of the island from this image. The N concentration as a function of distance from the closest edge is plotted in Figure 5D. In this sample, a linear gradient of N concentration is observed up to 60 nm from the edges, after which the N concentration reaches a plateau at the bulk value

of $\sim 0.4\%$. In addition to this N depletion at the graphene island edges, Figure 5C also shows a N depleted region in the nucleation region at the center of the graphene island, which is also observed in the Raman results in Figure 3A. Our STM results indicate that the basic phenomenology of dopants avoiding structural defects in graphene is independent of the details of the growth conditions such as temperature, pressure, and the precursor gases used. We however note that the length scale over which the dopants avoid edges and boundaries is not a universal number but depends on the size of the graphene grain with large depletion widths observed for the large grains.

Having shown the basic phenomenon of dopant inhomogeneity in N-doped graphene and excluded growth conditions as a factor of this observation, we consider briefly its consequences for the graphene film quality. Our measurements on even our best N-doped graphene films show variations in the G peak frequency between 1585 and 1592 cm^{-1} . This translates to an electronic doping in the graphene that varies from 2.0×10^{12} to $1.1 \times 10^{13} \text{ carriers/cm}^2$. This variation is a direct consequence of the N-dopant inhomogeneity and is also reflected in STM spectroscopy measurements, which show that the Dirac point can vary from the Fermi level to -400 meV in different areas of the same sample. Such electronic inhomogeneity is also reflected in the carrier concentration measured in graphene FETs made from N-doped graphene. Indeed, carrier concentration measured from transport devices is significantly (2–3 times smaller) than that measured from spectroscopy, indicating that the carriers show some degree of localization over the micron length scale (details in Supporting Information

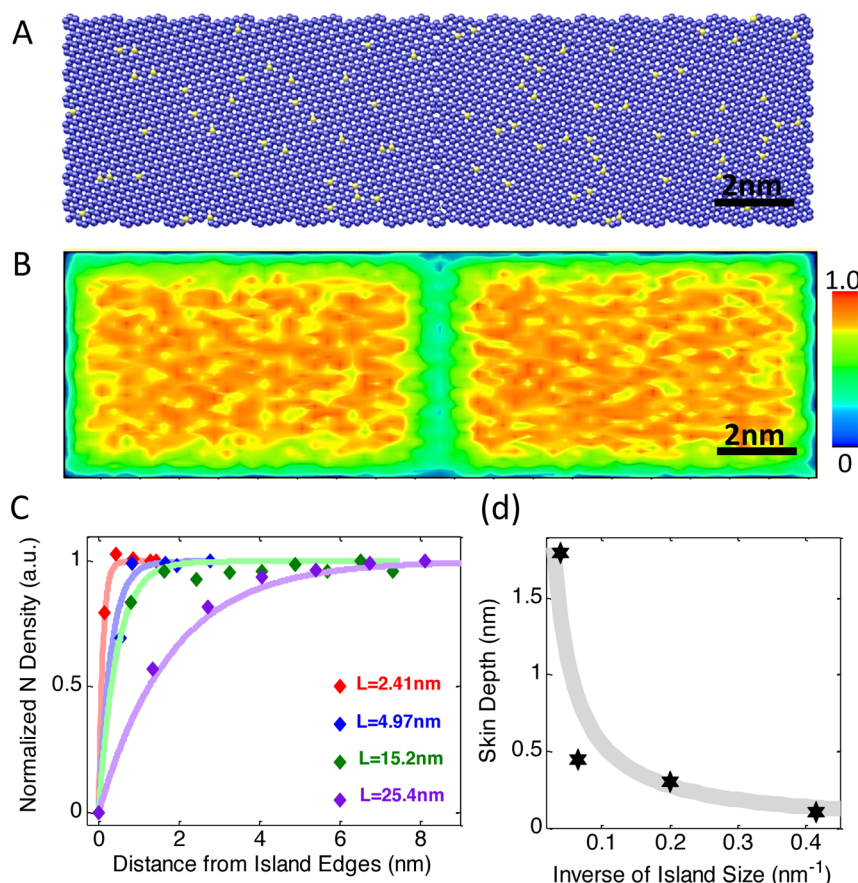


Figure 6. Monte Carlo simulations of dopant segregation in N-doped graphene. (A) Snapshot of simulated N distribution in an island of 19.2×5.9 nm² with a grain boundary inside. (B) N dopants density map (19.2×5.9 nm²) averaged over time. The vertical scale bar shows the N density calibrated to the maximum value of 1. (C) Dopant density profiles as a function of distance from the island edges for different graphene lattice size of 2.41×1.35 , 4.97×2.83 , 15.2×8.73 , and 25.4×14.6 nm². (D) Skin depths extracted from data in (C).

S9). All of these facts indicate that large-scale dopant inhomogeneity is a serious problem in electronics applications of functionalized 2D materials.

To gain further insight into the dopant inhomogeneity, we use Monte Carlo (MC) techniques to simulate the kinetics of dopants at high temperatures in a graphene sheet. Because the experimental conditions at the growth temperature are complex, we simulate various boundary conditions to obtain a comprehensive picture of the dopant kinetics (for full details of the MC calculation, see Supporting Information S10). The system's initial configuration involves random placement of the correct percentages of dopant at vertices in the lattice and the simulation is subsequently run at a temperature of $T = 1000$ K, where phase space is sampled using a standard Metropolis MC algorithm. In all cases studied, the system is first allowed to equilibrate for 100 000 steps, and the simulation is subsequently run out for a further 100 000 steps to study the behavior of nitrogen in the lattice after thermalization.

The snapshot in Figure 6A shows a typical configuration of dopant atoms in a graphene flake with a grain boundary inside. We compile all the snapshots of the dopant atom configurations taken during the production part of the simulations and generate an average density of nitrogen atoms in the sheet as shown in Figure 6B for multiple flake sizes. This figure clearly shows that the density of nitrogen atoms is reduced both near the edges of the sheet and around the grain boundary in the sheet, while it is relatively constant in

the interior of the sheet. To quantify this, we calculate the distance of all the dopant atoms from their nearest edges during the production part of the simulations and plot the density of the dopants as a function of the distance from the nearest edge in Figure 6C. We can see from this figure that the dopant density is indeed strongly reduced at the edge, and the length scale of this density reduction increases as a function of increasing system size. We extract a skin depth for each system size by fitting an exponential to the MC data. The extracted skin depth as a function of inverse system size is shown in Figure 6D. We note that the largest system we have considered is about 2 orders of magnitude smaller than the typical grain sizes seen in our experiments. Thus, we would not expect our skin depths to be directly comparable to the experimental values. However, it is encouraging that the skin depth trend seen in our simulations is consistent with the trend seen in the experiments, and a naïve extrapolation of the simulated skin depth is also consistent with experimental values. We note that the results for the static and relaxed lattices are almost indistinguishable, indicating that strain is playing a negligible role in the dopant inhomogeneity.

Our simulations do not address the effect of the substrate or the reaction kinetics of the true growth process where nitrogen and carbon atoms are present both on the surface and in the gas phase. While open questions still remain about the exact nature of the differences in the interatomic forces between N and C atoms that lead to the observed segregation, the fact that our

simulations are able to capture the essential quantitative behavior observed in the experiments without involving these additional complications indicate that the bonding and coordination energies of the N dopant in the graphene lattice play a key role in the observed phenomena. These general energetic considerations are expected to hold in any 2D system, and they present a challenge as well as an opportunity for creating new functionalized 2D materials.

■ ASSOCIATED CONTENT

Supporting Information

The material contains sample fabrication process (S1 and S2), XPS (S3), NEXAFS (S4), STM (S5 and S8), and transport (S9) measurements on samples, DFT calculations (S6), algorithm for estimating the width of N-depleted region near grain boundaries (S7), and Monte Carlo simulations (S10). This material is available free of charge via the Internet at <http://pubs.acs.org>.

■ AUTHOR INFORMATION

Corresponding Author

*E-mail: pasupathy@phys.columbia.edu.

Author Contributions

L.Z. and R.H. contributed equally.

Notes

The authors declare no competing financial interest.

■ ACKNOWLEDGMENTS

This material is based upon work supported as part of the Center for Re-Defining Photovoltaic Efficiency Through Molecule Scale Control, an Energy Frontier Research Center funded by the U.S. Department of Energy, Office of Basic Energy Science (DoE-BES) under Award Number DE-SC0001085. R.H. acknowledges support by a Provost's Pre-Tenure Summer Fellowship Award from the University of Northern Iowa and support by the American Chemical Society Petroleum Research Fund (No. 53401-UNI10). R.H. and A.P. acknowledge support by ONR (N000140610138 and Graphene MURI). Equipment support provided by National Science Foundation under Grant CHE-07-01483 and NSF CHE-10-12058 (G.W.F.). Sample fabrication supported by the Air Force Office of Scientific Research (AFOSR) Grant FA9550-11-1-0010 (L.Z., A.N.P.) and by Nano Material Technology Development Program through the National Research Foundation of Korea funded by the Ministry of Science, ICT and Future Planning (2012M3A7B4049966, P.K.). Salary support is provided by the DoE-BES under Grant DE-FG02-88ER13937 (G.W.F.) and by the AFOSR (MURI FA955009-1-0705, A. P.). Portions of this research were carried out at beamline U7A at the National Synchrotron Light Source, Brookhaven National Laboratory, which is supported by DoE-BES, under Contract No. DE-AC02-98CH10866.

■ REFERENCES

- Lejcek, P. *Springer Ser. Mater. Sci.* **2010**, *136*, 1–239.
- Bai, X.-M.; Voter, A. F.; Hoagland, R. G.; Nastasi, M.; Uberuaga, B. P. *Science* **2010**, *327* (5973), 1631–1634.
- Jia, C. L.; Urban, K. *Science* **2004**, *303* (5666), 2001–2004.
- Grovenor, C. R. M. *J. Phys. C: Solid State Phys.* **1985**, *18* (21), 4079.
- Maiti, A.; Chisholm, M. F.; Pennycook, S. J.; Pantelides, S. T. *Phys. Rev. Lett.* **1996**, *77* (7), 1306–1309.
- Inoue, K.; Yano, F.; Nishida, A.; Tsunomura, T.; Toyama, T.; Nagai, Y.; Hasegawa, M. *Appl. Phys. Lett.* **2008**, *93* (13), 133507–3.
- Seto, J. Y. W. *J. Appl. Phys.* **1975**, *46* (12), S247–S254.
- Mandurah, M. M.; Saraswat, K. C.; Helms, C. R.; Kamins, T. I. *J. Appl. Phys.* **1980**, *51* (11), S755–S763.
- Petroff, P. M.; Miller, R. C.; Gossard, A. C.; Wiegmann, W. *Appl. Phys. Lett.* **1984**, *44* (2), 217–219.
- Knoch, J.; Zhang, M.; Feste, S.; Mantl, S. *Microelectron. Eng.* **2007**, *84* (11), 2563–2571.
- Lee, W.; Han, J. W.; Chen, Y.; Cai, Z. H.; Yildiz, B. *J. Am. Chem. Soc.* **2013**, *135* (21), 7909–7925.
- Shao, Z. P.; Haile, S. M. *Nature* **2004**, *431* (7005), 170–173.
- Shaw, D.; Shaw, D. *Atomic diffusion in semiconductors*; Plenum Press: London, 1973; Vol. 255.
- Arias, T. A.; Joannopoulos, J. D. *Phys. Rev. B* **1994**, *49* (7), 4525–4531.
- Arias, T. A.; Joannopoulos, J. D. *Phys. Rev. Lett.* **1992**, *69* (23), 3330–3333.
- Huang, P. Y.; Ruiz-Vargas, C. S.; van der Zande, A. M.; Whitney, W. S.; Levendorf, M. P.; Kevek, J. W.; Garg, S.; Alden, J. S.; Hustedt, C. J.; Zhu, Y.; Park, J.; McEuen, P. L.; Muller, D. A. *Nature* **2011**, *469* (7330), 389–392.
- Kim, K.; Lee, Z.; Regan, W.; Kisielowski, C.; Crommie, M. F.; Zettl, A. *ACS Nano* **2011**, *5* (3), 2142–2146.
- Li, X.; Cai, W.; An, J.; Kim, S.; Nah, J.; Yang, D.; Piner, R.; Velamakanni, A.; Jung, I.; Tutuc, E.; Banerjee, S. K.; Colombo, L.; Ruoff, R. S. *Science* **2009**, *324* (5932), 1312–1314.
- Wei, D.; Liu, Y.; Wang, Y.; Zhang, H.; Huang, L.; Yu, G. *Nano Lett.* **2009**, *9* (5), 1752–1758.
- Jin, Z.; Yao, J.; Kittrell, C.; Tour, J. M. *ACS Nano* **2011**, *5* (5), 4112–4117.
- Zhao, L.; Levendorf, M.; Goncher, S.; Schiros, T.; Pálóvá, L.; Zabet-Khosousi, A.; Rim, K. T.; Gutiérrez, C.; Nordlund, D.; Jaye, C.; Hybertsen, M.; Reichman, D.; Flynn, G. W.; Park, J.; Pasupathy, A. N. *Nano Lett.* **2013**, *13* (10), 4659–4665.
- Song, L.; Ci, L.; Lu, H.; Sorokin, P. B.; Jin, C.; Ni, J.; Kvashnin, A. G.; Kvashnin, D. G.; Lou, J.; Yakobson, B. I.; Ajayan, P. M. *Nano Lett.* **2010**, *10* (8), 3209–3215.
- Kim, K. K.; Hsu, A.; Jia, X. T.; Kim, S. M.; Shi, Y. S.; Hofmann, M.; Nezich, D.; Rodriguez-Nieva, J. F.; Dresselhaus, M.; Palacios, T.; Kong, J. *Nano Lett.* **2012**, *12* (1), 161–166.
- Liu, K.-K.; Zhang, W.; Lee, Y.-H.; Lin, Y.-C.; Chang, M.-T.; Su, C.-Y.; Chang, C.-S.; Li, H.; Shi, Y.; Zhang, H.; Lai, C.-S.; Li, L.-J. *Nano Lett.* **2012**, *12* (3), 1538–1544.
- van der Zande, A. M.; Huang, P. Y.; Chenet, D. A.; Berkelbach, T. C.; You, Y.; Lee, G.-H.; Heinz, T. F.; Reichman, D. R.; Muller, D. A.; Hone, J. C. *Nat. Mater.* **2013**, *12* (6), S54–S61.
- Gong, Y. J.; Liu, Z.; Lupini, A. R.; Shi, G.; Lin, J. H.; Najmaei, S.; Lin, Z.; Elias, A. L.; Berkdemir, A.; You, G.; Terrones, H.; Terrones, M.; Vajtai, R.; Pantelides, S. T.; Pennycook, S. J.; Lou, J.; Zhou, W.; Ajayan, P. M. *Nano Lett.* **2014**, *14* (2), 442–449.
- Tringides, M. C. *Surface Diffusion: Atomistic and Collective Processes*; Springer: New York, 1997; Vol. 360.
- Tsong, T. T. *Prog. Surf. Sci.* **2001**, *67* (1–8), 235–248.
- Meyer, J. C.; Kurasch, S.; Park, H. J.; Skakalova, V.; Künzel, D.; Groß, A.; Chuvilin, A.; Algara-Siller, G.; Roth, S.; Iwasaki, T.; Starke, U.; Smet, J. H.; Kaiser, U. *Nat. Mater.* **2011**, *10* (3), 209–215.
- Zhao, L.; He, R.; Rim, K. T.; Schiros, T.; Kim, K. S.; Zhou, H.; Gutiérrez, C.; Chockalingam, S. P.; Arguello, C. J.; Pálóvá, L.; Nordlund, D.; Hybertsen, M. S.; Reichman, D. R.; Heinz, T. F.; Kim, P.; Pinczuk, A.; Flynn, G. W.; Pasupathy, A. N. *Science* **2011**, *333* (6045), 999–1003.
- Lv, R.; Li, Q.; Botello-Méndez, A. R.; Hayashi, T.; Wang, B.; Berkdemir, A.; Hao, Q.; Elías, A. L.; Cruz-Silva, R.; Gutiérrez, H. R.; Kim, Y. A.; Muramatsu, H.; Zhu, J.; Endo, M.; Terrones, H.; Charlier, J.-C.; Pan, M.; Terrones, M. *Sci. Rep.* **2012**, *2*, 586.
- Joucken, F.; Tison, Y.; Lagoute, J.; Dumont, J.; Cabosart, D.; Zheng, B.; Repain, V.; Chacon, C.; Girard, Y.; Botello-Méndez, A. R.

- Rousset, S.; Sporken, R.; Charlier, J.-C.; Henrard, L. *Phys. Rev. B* **2012**, *85* (16), 161408.
- (33) Schiros, T.; Nordlund, D.; Pálóvá, L.; Prezzi, D.; Zhao, L.; Kim, K. S.; Wurstbauer, U.; Gutiérrez, C.; Delongchamp, D.; Jaye, C.; Fischer, D.; Ogasawara, H.; Pettersson, L. G. M.; Reichman, D. R.; Kim, P.; Hybertsen, M. S.; Pasupathy, A. N. *Nano Lett.* **2012**, *12* (8), 4025–4031.
- (34) Casiraghi, C.; Pisana, S.; Novoselov, K. S.; Geim, A. K.; Ferrari, A. C. *Appl. Phys. Lett.* **2007**, *91* (23), 233108–3.
- (35) Ferrari, A. C. *Solid State Commun.* **2007**, *143* (1–2), 47–57.
- (36) Malard, L. M.; Pimenta, M. A.; Dresselhaus, G.; Dresselhaus, M. S. *Phys. Rep.* **2009**, *473* (5–6), 51–87.
- (37) Pimenta, M. A.; Dresselhaus, G.; Dresselhaus, M. S.; Cancado, L. G.; Jorio, A.; Saito, R. *Phys. Chem. Chem. Phys.* **2007**, *9* (11), 1276–1290.
- (38) Ferrari, A. C.; Basko, D. M. *Nat. Nanotechnol.* **2013**, *8* (4), 235–246.
- (39) Cançado, L. G.; Pimenta, M. A.; Neves, B. R. A.; Dantas, M. S.; Jorio, A. *Phys. Rev. Lett.* **2004**, *93* (24), 247401.
- (40) Casiraghi, C.; Hartschuh, A.; Qian, H.; Piscanec, S.; Georgi, C.; Fasoli, A.; Novoselov, K. S.; Basko, D. M.; Ferrari, A. C. *Nano Lett.* **2009**, *9* (4), 1433–1441.
- (41) Eckmann, A.; Felten, A.; Mishchenko, A.; Britnell, L.; Krupke, R.; Novoselov, K. S.; Casiraghi, C. *Nano Lett.* **2012**, *12* (8), 3925–3930.
- (42) Kim, Y. A.; Fujisawa, K.; Muramatsu, H.; Hayashi, T.; Endo, M.; Fujimori, T.; Kaneko, K.; Terrones, M.; Behrends, J.; Eckmann, A.; Casiraghi, C.; Novoselov, K. S.; Saito, R.; Dresselhaus, M. S. *ACS Nano* **2012**, *6* (7), 6293–6300.
- (43) Yan, J.; Zhang, Y.; Kim, P.; Pinczuk, A. *Phys. Rev. Lett.* **2007**, *98* (16), 166802.
- (44) Das, A.; Pisana, S.; Chakraborty, B.; Piscanec, S.; Saha, S. K.; Waghmare, U. V.; Novoselov, K. S.; Krishnamurthy, H. R.; Geim, A. K.; Ferrari, A. C.; Sood, A. K. *Nat. Nanotechnol.* **2008**, *3* (4), 210–215.
- (45) Mohiuddin, T.; Lombardo, A.; Nair, R.; Bonetti, A.; Savini, G.; Jalil, R.; Bonini, N.; Basko, D.; Galiotis, C.; Marzari, N. *Phys. Rev. B* **2009**, *79* (20), 205433.
- (46) He, R.; Zhao, L.; Petrone, N.; Kim, K. S.; Roth, M.; Hone, J.; Kim, P.; Pasupathy, A.; Pinczuk, A. *Nano Lett.* **2012**, *12* (5), 2408–2413.
- (47) Zheng, B.; Hermet, P.; Henrard, L. *ACS Nano* **2010**, *4* (7), 4165–4173.
- (48) Maciel, I. O.; Anderson, N.; Pimenta, M. A.; Hartschuh, A.; Qian, H.; Terrones, M.; Terrones, H.; Campos-Delgado, J.; Rao, A. M.; Novotny, L.; Jorio, A. *Nat. Mater.* **2008**, *7* (11), 878–883.
- (49) Zafar, Z.; Ni, Z. H.; Wu, X.; Shi, Z. X.; Nan, H. Y.; Bai, J.; Sun, L. T. *Carbon* **2013**, *61* (0), 57–62.
- (50) Park, S. H.; Chae, J.; Cho, M.-H.; Kim, J. H.; Yoo, K.-H.; Cho, S. W.; Kim, T. G.; Kim, J. W. *J. Mater. Chem. C* **2014**, *2* (5), 933–939.
- (51) Usachov, D.; Vilkov, O.; Grüneis, A.; Haberer, D.; Fedorov, A.; Adamchuk, V. K.; Preobrajenski, A. B.; Dudin, P.; Barinov, A.; Oehzelt, M.; Laubschat, C.; Vyalikh, D. V. *Nano Lett.* **2011**, *11* (12), 5401–5407.
- (52) Lucchese, M. M.; Stavale, F.; Ferreira, E. H. M.; Vilani, C.; Moutinho, M. V. O.; Capaz, R. B.; Achete, C. A.; Jorio, A. *Carbon* **2010**, *48* (5), 1592–1597.
- (53) Cançado, L. G.; Jorio, A.; Ferreira, E. H. M.; Stavale, F.; Achete, C. A.; Capaz, R. B.; Moutinho, M. V. O.; Lombardo, A.; Kulmala, T. S.; Ferrari, A. C. *Nano Lett.* **2011**, *11* (8), 3190–3196.
- (54) Venezuela, P.; Lazzeri, M.; Mauri, F. *Phys. Rev. B* **2011**, *84* (3), 035433.
- (55) Vlassiuk, I.; Regmi, M.; Fulvio, P.; Dai, S.; Datskos, P.; Eres, G.; Smirnov, S. *ACS Nano* **2011**, *5* (7), 6069–6076.
- (56) Yu, Q.; Jauregui, L. A.; Wu, W.; Colby, R.; Tian, J.; Su, Z.; Cao, H.; Liu, Z.; Pandey, D.; Wei, D.; Chung, T. F.; Peng, P.; Guisinger, N. P.; Stach, E. A.; Bao, J.; Pei, S.-S.; Chen, Y. P. *Nat. Mater.* **2011**, *10* (6), 443–449.
- (57) Duong, D. L.; Han, G. H.; Lee, S. M.; Gunes, F.; Kim, E. S.; Kim, S. T.; Kim, H.; Ta, Q. H.; So, K. P.; Yoon, S. J.; Chae, S. J.; Jo, Y. W.; Park, M. H.; Chae, S. H.; Lim, S. C.; Choi, J. Y.; Lee, Y. H. *Nature* **2012**, *490* (7419), 235–239.
- (58) Zhao, L.; Rim, K. T.; Zhou, H.; He, R.; Heinz, T. F.; Pinczuk, A.; Flynn, G. W.; Pasupathy, A. N. *Solid State Commun.* **2011**, *151* (7), 509–513.